

BU/HEPP/96-01

June 1996

hep-lat/9502015(revised)

Lattice Charge Overlap I: Elastic Limit of Pi and Rho Mesons

William Andersen*Department of Physics, Eastern New Mexico University, Portales, NM 88130***Walter Wilcox***Department of Physics, Baylor University, Waco, TX 76798-7316*

Abstract

Using lattice QCD on a $16^3 \times 24$ lattice at $\beta = 6.0$, we examine the elastic limit of charge overlap functions in the quenched approximation for the pion and rho meson; results are compared to previous direct current insertion calculations. A good signal is seen for the pion, but the electric and magnetic rho meson results are considerably noisier. We find that the pion and rho results are characterized by a monopole mass to rho mass ratio of 0.97(8) and 0.73(10), respectively. Assuming the functional form of the electric and magnetic form factors are the same, we also find a rho meson g-factor of $g = 2.25(34)$, consistent with the nonrelativistic quark model.

I. INTRODUCTION

The spacelike pion form factor has been the subject of a number of completed lattice studies [1–3]. However, it has not yet been studied systematically by the method of Ref. [4]. It would be helpful to compare the systematic and statistical characteristics of current overlap to previous results as well as to learn about possible limitations. Since the same set of quark propagators can also be used to construct current overlap functions for higher spin, we investigate the rho meson as well. As was the case with the decouplet baryons studied in Ref. [5], the rho meson is not stable under the strong interactions. However, at quark masses available in lattice calculations, its decay is kinematically forbidden, so in this sense our quenched results are physical. Another motivating factor in studying the rho is to have a more “typical” hadron to compare our pion results to, especially in terms of the relative statistical signals. Our results can also be used to compare to hadronic models.

Current overlap techniques are versatile in that the same set of quark propagators can be used to study both elastic and inelastic processes. In the second part of this series, referred to as Part II, the inelastic part of the correlation functions calculated here will be used to partially address the question of the polarizability of the charged pion. Thus, another purpose of the present study is to set the elastic “baseline” necessary to extract additional nonelastic properties of hadrons. In addition to polarizability, structure functions may also be extracted using these techniques [4,6].

In summary, the purpose of this study and others like it is both as a testing ground for lattice techniques and as a preliminary contact between experiment and fundamental theory. As we explore the numerics, we will be more interested in trends in our lattice data rather than the final numbers. Nevertheless, we do not neglect comparison wherever possible to previous lattice and experimental results. We will partially explore the systematics associated with longer time correlations, larger volume and finite lattice spacing effects. However, further work treating systematic effects such as scaling and quenching will need to be done before our numerical results can be accepted as “physical”.

We will start with a review of the formulas used in this study and then proceed directly to the results. We finish with a summary and some brief comments about the possible physics underlying our results.

II. CORRELATION FUNCTIONS

A. Formulas

The formulas necessary for measuring the form factors of the pion and rho meson by the current overlap technique have been developed in Ref. [7]. The relevant results are the following. One can define the u, d flavor charge and current density overlap matrix elements (continuum, imaginary time formalism) for these two particles as :

$$P(\vec{r}, t) \equiv \frac{1}{2m_\pi} (\pi^+(\mathbf{0}) | T[-\rho^d(\vec{r}, t) \rho^u(0)] | \pi^+(\mathbf{0})), \quad (1)$$

$$P(\xi; \vec{r}, t) \equiv \frac{1}{2m_\rho} (\rho^+(\xi; \mathbf{0}) | T[-\rho^d(\vec{r}, t) \rho^u(0)] | \rho^+(\xi; \mathbf{0})), \quad (2)$$

$$J_k(\xi; \vec{r}, t) \equiv \frac{1}{2m_\rho} (\rho^+(\xi; \mathbf{0}) | T[-\rho^d(\vec{r}, t) J_k^u(0)] | \rho^+(\xi; \mathbf{0})). \quad (3)$$

$\rho^{u,d}(\vec{r}, t)$ represents the charge density operator ($J_\mu = (\vec{J}, i\rho)$); $\rho^+(\xi; \mathbf{0})$ represents the vector particle state of spin polarization ξ ($\xi = \pm, 0$ refers to spin component along the z-axis) and zero momentum. We define the Fourier transforms:

$$Q(\vec{q}^2, t) \equiv \int d^3r e^{i\vec{x}\cdot\vec{q}} P(\vec{r}, t), \quad (4)$$

$$Q(\xi; \vec{q}^2, t) \equiv \int d^3r e^{i\vec{x}\cdot\vec{q}} P(\xi; \vec{r}, t), \quad (5)$$

$$K_k(\xi; \vec{q}, t) \equiv \int d^3r e^{i\vec{x}\cdot\vec{q}} J_k(\xi; \vec{r}, t). \quad (6)$$

In the large Euclidean time limit we can design form factor measurements from the amplitudes (“a” is the lattice spacing)

$$Q(\vec{q}^2, t) \xrightarrow{t \gg a} \frac{(E_q + m_\pi)^2}{4E_q m_\pi} F_\pi^2(q^2) e^{-(E_q - m_\pi)t}, \quad (7)$$

$$Q(\pm; q_z^2, t) \xrightarrow{t \gg a} \frac{(E_q + m_\rho)^2}{4E_q m_\rho} G_\rho^2(\pm; q_z^2) e^{-(E_q - m_\rho)t}, \quad (8)$$

$$Q(0; q_{x,y}^2, t) \xrightarrow{t \gg q} \frac{(E_q + m_\rho)^2}{4E_q m_\rho} G_\rho^2(0; q_{x,y}^2) e^{-(E_q - m_\rho)t}, \quad (9)$$

$$Q(\pm; q_{x,y}^2, t) \xrightarrow{t \gg q} \frac{(E_q + m_\rho)^2}{4E_q m_\rho} G_\rho^2(\pm; q_{x,y}^2) e^{-(E_q - m_\rho)t}, \quad (10)$$

$$K_y(+; q_x, t) \xrightarrow{t \gg q} i q_x \frac{(E_q + m_\rho)}{4E_q m_\rho} H_\rho(+; q_x^2) e^{-(E_q - m_\rho)t}. \quad (11)$$

F_π is the pion electric form factor and one can show that $G_\rho(\pm; q_z^2) = G_\rho(0; q_{x,y}^2)$. In Eq.(11) we may cyclically change the directions of the current, polarization and momentum; anticyclic changes produce a minus sign. We can then extract the charge (G_c), quadrupole (G_q) and magnetic (G_m) form factors of the rho meson from (the common magnitude of spatial momentum is \bar{q})

$$G_c = G_\rho(\pm; q_z^2) \left(\frac{2}{3} + \frac{1}{3}\eta \right), \quad (12)$$

$$G_q = \frac{m(E_q + m)}{\bar{q}^2} G_\rho(\pm; q_z^2) (-1 + \eta), \quad (13)$$

$$G_m = \frac{2H_\rho(+; q_x^2)}{G_\rho(\pm; q_z^2) (1 + \eta)}, \quad (14)$$

where

$$\eta \equiv \left(2 \frac{G_\rho^2(\pm; q_{x,y}^2)}{G_\rho^2(\pm; q_z^2)} - 1 \right)^{1/2}. \quad (15)$$

B. Simulation Details

Our quenched lattices were constructed by the algorithm in Ref. [8], thermalized by 11000 sweeps, and separated by 1000 sweeps. (Ten of these lattices overlap with those used in Ref. [9].) Our results are obtained with Wilson fermions on twenty $16^3 \times 24$ lattices at $\beta = 6.0$. We used the exactly conserved lattice charge and current densities in forming the overlaps. For the quarks, we used periodic boundary conditions in space and “fixed” boundary conditions in time (lattice time boundary gauge field time links are unused). When a particular polarization and momentum state is called for in the above, we measure this in all possible ways in a given configuration in order to reinforce the signal. For example,

the $G_\rho(\pm; q_z^2)$ amplitude can be measured by averaging the results for $\xi = \pm$. An additional two measurements are afforded by $G_\rho(0; q_{x,y}^2)$. When a correlation function for the second momentum is constructed, we combine signals from $\vec{q} = (\pm\frac{\pi}{8}, \pm\frac{\pi}{8}, 0)$, $(\pm\frac{\pi}{8}, 0, \pm\frac{\pi}{8})$ and $(0, \pm\frac{\pi}{8}, \pm\frac{\pi}{8})$.

In forming these amplitudes on the lattice, we neglect the charge and current self-contraction loops, which do not vanish in this context. In terms of quark lines, these are the disconnected (sea quark) diagrams, which are extremely difficult to simulate¹. However, it is unlikely that such local objects will significantly affect the elastic (large time separation) limit studied here. The connected amplitude and an example of a disconnected contribution are shown in Figs.1(a) and (b), respectively. In collecting data from our propagators, we do so in a manner which is as symmetrical as possible in time, given that the conserved lattice charge density is nonlocal. Thus, we use the symmetrized charge density, $\frac{1}{2}[\rho(\vec{r}, t) + \rho(\vec{r}, t - 1)]$, naturally associated with integer time locations, in forming the $H_\rho(\xi; \vec{q}^2)$ correlations. In addition, we find it is important to locate the two currents as symmetrically as possible between the particle interpolation fields, which are fixed in time. When a symmetrical time array of currents is not possible, we average over the two possibilities on each configuration. The time behavior of our signals is then much smoother.

Our lattice interpolation fields for the pion and rho are standard, given by $\bar{\psi}^d \gamma_5 \psi^u$ and $\bar{\psi}^d \epsilon_i(\xi) \gamma_i \psi^u$, where $\hat{\epsilon}(\pm) = \frac{1}{\sqrt{2}}(\mp \hat{x} - i \hat{y})$, $\hat{\epsilon}(0) = \hat{z}$ (rho meson rest frame). However, our interpolation fields are smeared over the entire lattice spatial volume (using the lattice Coulomb gauge), projecting onto zero momentum. Form factors are calculated at three values of the hopping parameter ($\kappa = 0.148, 0.152$ and 0.154) and parameters are extrapolated linearly to the chiral limit.

The lattice analog of the coordinate space functions $P(\vec{r}, t)$, $P(\xi; \vec{r}, t)$ and $J_k(\xi; \vec{r}, t)$, which we shall denote as $\mathcal{P}(\vec{r}, t)$, $\mathcal{P}(\xi; \vec{r}, t)$ and $\mathcal{J}_k(\xi; \vec{r}, t)$, can be shown to be real and purely imaginary, respectively, in the configuration average. That is, using the identity developed in Ref. [10] and given that the gauge fields U and U^* appear with equal weight in the ensemble average, one may show that

$$\mathcal{P}(\vec{r}, t; \{U\}) = \mathcal{P}(\vec{r}, t; \{U^*\})^*, \quad (16)$$

$$\mathcal{P}(\xi; \vec{r}, t; \{U\}) = \mathcal{P}(\xi; \vec{r}, t; \{U^*\})^*, \quad (17)$$

and

$$\mathcal{J}_k(\xi; \vec{r}, t; \{U\}) = -\mathcal{J}_k(\xi; \vec{r}, t; \{U^*\})^*. \quad (18)$$

These identities allow us to neglect terms which are purely noise in the discrete Fourier transforms of $\mathcal{P}(\vec{r}, t; \{U\})$, $\mathcal{P}(\xi; \vec{r}, t; \{U\})$ and $\mathcal{J}_k(\xi; \vec{r}, t; \{U\})$. ($\mathcal{P}(\vec{r}, t)$, $\mathcal{P}(\xi; \vec{r}, t)$ and $\mathcal{J}_k(\xi; \vec{r}, t)$ are clearly bad notation for these four-point functions which obviously depend on more than just the relative spatial and time separations. However, Eqs.(16)-(18) convey the basic idea.) Also, by combining Fourier transform measurements involving both \vec{q} and $-\vec{q}$ as we do, one is explicitly symmetrizing or antisymmetrizing these, so there is no need to assume evenness or oddness in \vec{r} . We can actually show that the identities,

$$\mathcal{P}(\vec{r}, t) = \mathcal{P}(-\vec{r}, t)^*, \quad (19)$$

$$\mathcal{P}(\xi; \vec{r}, t) = \mathcal{P}(\xi; -\vec{r}, t)^*, \quad (20)$$

hold exactly, configuration by configuration, for the lattice charge overlap functions. We can find no corresponding exact statement for $\mathcal{J}_k(\xi; \vec{r}, t)$, however.

One important aspect of forming the overlap functions is to have an efficient algorithm for sewing together the quark lines to form the charge and current densities at all relative spatial separations. Our analysis codes use the following trick to save computer time. The inner loop has a sum that looks like:

$$f(\vec{r}) = \sum_{\vec{x}} f_2(\vec{x} + \vec{r}) f_1(\vec{x}). \quad (21)$$

(\vec{x} , \vec{r} are spatial locations in a cubic 3D space.) This loop, which scales like N_s^2 , where N_s is the number of space points in the lattice, and must be repeated at all chosen relative time separations, is not easily vectorizable for spatially periodic boundary conditions. This equation was replaced by a version using Fourier transforms:

$$f(\vec{r}) = \sum_{\vec{q}} e^{-i\vec{q}\cdot\vec{r}} Q2(-\vec{q})Q1(\vec{q}), \quad (22)$$

where

$$Q1(\vec{q}) = \sum_{\vec{x}_1} e^{-i\vec{q}\cdot\vec{x}_1} f1(\vec{x}_1), \quad (23)$$

$$Q2(-\vec{q}) = \sum_{\vec{x}_2} e^{i\vec{q}\cdot\vec{x}_2} f2(\vec{x}_2). \quad (24)$$

This version is easily vectorized (i.e., the $Q2(-\vec{q})$ times $Q1(\vec{q})$ above) and can utilize fast Fourier transform routines². This technique allows us to extract, with only a small amount of computer time, the full time extent of the current overlap correlations, even up to $t = 22$, where the currents begin to overlap with the interpolation fields.

In making our choice of fits to masses and correlation functions, we examine the chi-squared per degree of freedom, χ_d^2 , using correlated fits. The covariance matrix [11], C_{ij} , is estimated from the single-elimination jackknife [12,13]:

$$C_{ij} = \frac{N-1}{N} \sum_{n=1}^N (X_i(n) - \hat{X}_i)(X_j(n) - \hat{X}_j), \quad (25)$$

where N is the number of configurations, i and j label different time slices, and the $X_i(n)$ represent jackknifed propagator data, \hat{X}_i being the average to remove the bias. The χ^2 is then given by

$$\chi^2 = \sum_{i,j} C_{ij}^{-1} (\bar{Y}_i - f_i)(\bar{Y}_j - f_j), \quad (26)$$

where the \bar{Y}_i are the average experimental values of the propagators and the f_i are the functional form values for these time slices. However, it has been noticed by many authors that the covariance matrix overestimates correlations on propagators for small numbers of configurations [14]. Therefore our procedure on fits is the following. We choose our time intervals based upon obtaining acceptable values of the χ_d^2 . However, following the suggestion in Ref. [14], the actual fits themselves are uncorrelated, which simply means neglecting the off-diagonal components of the C_{ij} . We feel it is necessary, and will see later it can be important, to take correlations into account in extrapolating our results across κ values.

Therefore, the full forms of Eqs.(25), (26) are used in our chiral extrapolations (i, j then label κ values).

A third order single elimination jackknife was used for error analysis; the first order defines error bars on the time correlation functions, the second defines error bars on the time correlation fits and the third is necessary for the chiral extrapolation of the results. Our masses were measured on twenty gauge configurations using single exponential fits and are listed in Table I along with the chi-squared per degree of freedom, χ_d^2 , of the fit. The source position for these propagators is the first time slice of the lattice ($t \equiv 0$). The masses are consistent with those measured with twelve configurations in Ref. [9]. However, in order to find a time interval on which the correlated χ_d^2 was acceptable for our pi and rho masses simultaneously, we had to increase the time interval considerably beyond the fits in this reference, resulting in slightly increased error bars.

Two definitions for the Wilson quark mass, which agree for $\kappa \approx \kappa_c$, have been used in previous studies of form factors. These definitions are

$$ma = \frac{1}{2} \left(\frac{1}{\kappa} - \frac{1}{\kappa_c} \right), \quad (27)$$

and

$$ma = \ln \left(\frac{4\kappa_c}{\kappa} - 3 \right), \quad (28)$$

where κ_c is the critical κ value for which the pion mass vanishes. The first definition is motivated by leading order chiral perturbation theory; the second definition comes from tadpole improving [15] the quark pole mass in free field theory. Fitting the square of the pion mass in Table I with Eq.(27) gives $\kappa_c = 0.1566(2)$. (Ref. [13] gives $\kappa_c = 0.1570(1) \pm .0002$ from $t = 9$ to 14 point-source fits, whereas the fits here are $t = 15$ to 18 smeared-source. See the next section for more comments on our time fit choice.) Fitting the same data to Eq.(28) gives $\kappa_c = 0.1564(2)$. We prefer Eq.(28) and the latter κ_c value in this work to partly correct for the fact that our quark masses may not be in the leading order chiral limit range.

As was done in Ref. [9], we shall concentrate here on dimensionless quantities in extrapolating to the chiral limit. This is because a ratio of similar physical quantities is often less subject to systematic errors. Our philosophy in comparing our results to experiment is to assume the simplest possible functional form and to extrapolate the fit parameters rather than individual form factor values in order to make contact with phenomenology. This is crucial in the case of the pion, where the four momentum transfer in the chiral limit vanishes.

III. RESULTS

A. Preliminaries

First, let us make a point about our correlation functions, which are four-point functions. In order to measure current overlap functions, it is necessary to form an amplitude which looks generically like Fig.1(a). Eqs.(7)-(11) tell us the form factors are identified in the large time separation limit, t , of the charge or current densities. However, large time separation between the currents produces small time separation between the fixed interpolation fields and the currents. It is only as we increase the time separations between all four time locations of our four-point function that the lattice amplitudes project with increasing accuracy on the ground state. This is quite different from generic two-point functions which, outside of time boundary effects, are guaranteed to have a better ground state overlap for larger time separations. This has important implications for our time fits, as we will discuss below.

We next discuss two tests done to help motivate the choices made in this study regarding the use of smeared fields and for the time position of the interpolation fields.

One test is given in Fig.2(a), which shows a graph of the Fourier transform of the equal-time charge overlap function, $Q(\vec{q}^2, t)$, as both charge densities are moved *in unison* between pion source and sink at $\kappa = 0.154$. This measurement is associated with half-integer time steps since the conserved lattice current is non-local in time. We are using smeared-to-smeared quark fields and are examining the two lowest momenta on a linear scale using

twenty configurations. The data should be flat if the lattice is long enough in time. The satisfactory results seen in Fig.2(a) are to be contrasted with those in Fig.2(b), which repeat the same measurement (using a subset of ten configurations), but using smeared-to-point³ correlation functions.

Having adopted smeared fields, in Fig.3 we show measurements of the Fourier transform of the pion overlap distribution functions, $Q(\vec{q}^2, t)$, on a \log_{10} scale at the two lowest spatial momenta transfer for $\Delta T = 17$ (boxes) and $\Delta T = 23$ (diamonds), again at $\kappa = 0.154$. ΔT refers to the time separation of the pion source and sink fields; time separations between the charge densities range from 0 to 10. (The $\Delta T = 17$ time correlation data is from Ref. [4], where only charge overlap time separations up to 10 were considered because of the expensiveness of constructing the overlap function. See Section II(B) above for comments on the improved method used here.) Note that the $\Delta T = 17$ measurements use twelve configurations and the $\Delta T = 23$ use twenty, ten of which overlap. There are no significant differences within statistical errors for the lowest momentum (upper set of points), but there appears to be a difference larger than the error bars on the second momentum results. To examine the situation from another point of view, consider Figs.4(a) and (b). Here we have plotted the local $(E - m)$ determined from the exponential falloff of the pion overlap function for the three κ values in this study in (a) for $|\vec{q}_{min}| = \frac{\pi}{8}$ and (b) for $|\vec{q}| = \sqrt{2}|\vec{q}_{min}|$. This measurement is also naturally associated with half-integer time values. Although the different κ values approach the asymptotic limit at different rates, all of the first momentum results are quite consistent with the expected exponential falloff (determined from continuum dispersion and the measured pion mass) by a time separation of 14 steps. The second momentum results in Fig.4(b) are more problematical. The $\kappa = 0.154$ local $(E - m)$ results are seen to eventually approach the correct asymptotic falloff (slower than for the first momentum), albeit with large error bars. However, the smallest κ value at this larger momentum is apparently displaying a violation of continuum dispersion. (The dotted lines in Figs.4(a) and (b) give the spin 0 lattice result; see Eq.(31) below.) Because of this *apparent* violation we prefer in this study to exclude higher momentum measurements for

both the pion and rho meson. (We will estimate the remaining effect of finite lattice spacing on our first momentum extrapolated quantities at the end of the next section.) An analysis of the lowest momentum rho meson local electric ($E - m$) shows a similar pattern to the pion with, however, larger errors. In addition, we will see later that the rho meson magnetic ($E - m$) becomes consistent with continuum dispersion much earlier in time than the electric ones. Thus, our lattice appears to have enough time steps to filter out asymptotic limit of the first momentum in the overlap correlation functions and continuum dispersion is reliable within errors.

B. Numerical Results

After these preliminaries, we now begin with a survey of the correlation functions measured in this study, given by the quantities in Eqs.(7)-(11). The different κ values are combined and shown in Figs.5-8. We will take some pains to examine all the correlation functions since this is the first complete study using the current overlap technique.

First, let us explain our fitting procedure. As pointed out above, large time separations of the currents move them toward the interpolation fields, fixed at the time ends of the lattice. There is no *á priori* reason that the large time separation amplitudes are to be favored; non ground state contributions are expected both for small as well as for large time separations. We will use the calculated χ_d^2 of the fits to determine allowed fit time intervals for the correlation functions. In our fits, we wish to extend the time plateaus sufficiently that we are testing the fit in a nontrivial way, but not so extended that the χ_d^2 becomes unmanageable or the statistical signal has decayed. Our choice of fitting 3 time values on overlap functions and 4 on mass correlation functions is thus a compromise between systematics and statistics. (Both types of fits involve 2 independent degrees of freedom.) Our overlap fits will assume the continuum dispersion relation, $E^2 = \vec{q}^2 + m^2$. We attempt to fit all κ values for given type of correlation function on the same time interval in order to increase possible correlations across κ . We find this to be a significant effect for the chiral

extrapolation of the pion data. (See the discussion under Fig.9 below.)

Fig.5 shows the correlation functions, $Q(\vec{q}^2, t)$ versus time separation, t , for the pion. (The next 4 figures are \log_{10} plots.) The lines drawn are the best fits over a common $t = 14$ to 16 time separation interval. A single exponential form is evident even for large time separations. The form factors, F , from these fits using Eq.(7) are listed in Table II along with the implied F/F^{VD} ratio (F^{VD} is the vector dominance result predicted by the masses in Table I) and the χ_d^2 . Notice that all of the F/F^{VD} ratios are low compared to the vector dominance result of 1.

Fig.6 shows the time separation correlation function for the rho meson corresponding to adding the signals for $Q(\pm; q_z^2, t)$ and $Q(0; q_{x,y}^2, t)$ (see Eqs.(8) and (9).) The error bars are significantly larger than for the pion. The $\kappa = 0.148$ and 0.152 results are fit across $t = 14$ to 16 (as for the pion) with acceptable χ_d^2 values; see the χ_d^2 values in Table IV under the line for G_c/G^{VD} . However, a similar fit to the $\kappa = 0.154$ data gives a rather large value for χ_d^2 (1.99) caused by poor exponential behavior near the time separation edge. We have therefore moved this fit inward until an acceptable fit is achieved. This occurs after shifting it a single time step ($t = 13$ to 15 fit); we now have $\chi_d^2 = 0.43$. We note that the local $(E - m)$ values for $\kappa = 0.154$ are low, but consistent within large error bars with continuum dispersion across these time slices; the other two κ values are also consistent in this sense.

Fig.7 shows the magnetic correlation function $K_y(+; q_x, t)$ as a function of time separation. The time behavior of these functions, which come from charge-current overlap (see Eqs.(3) and (6)), is quite different from the electric (charge-charge overlap) functions just examined. We are able to fit these functions much earlier in time to the required exponential behavior with acceptable χ_d^2 values than in Figs.5 or 6, resulting in improved error bars. The situation is similar to the magnetic correlation functions for the proton, examined in Ref. [9], which also assumed their expected exponential behavior more quickly than their electric counterparts. The χ_d^2 values of these fits are listed in Table IV (under the line for G_m). Again, the local $(E - m)$ values across the chosen time slices are consistent within error bars with continuum dispersion.

Fig.8 shows the rho correlation function $Q(\pm; q_{x,y}^2, t)$ as a function of time separation. There seems to be a nonexponential systematic effect for larger time separations for $\kappa = 0.152$ and $\kappa = 0.154$. In addition, the local $(E - m)$ plots for these κ values are never consistent within error bars with the expected exponential falloff. We feel that the appropriate conclusion from these difficulties is that the quadrupole form factor can not be reliably extracted with our data sample. We note that if the quadrupole form factor is zero, the results in Figs.6 and 8 should be the same within statistical errors for each κ value; there is indeed strong overlap of the error bars. Therefore, in what is to follow, we assume that $G_q(q^2) = 0$, consistent with the data⁴. In Eqs.(12)-(14) this makes $\eta = 1$. The values for the electric, G_c , and magnetic, G_m , form factors in Table IV were extracted with this assumption.

Now that we have examined the correlation functions, in Fig.9 we begin to show results of extrapolations of the pion correlation functions. The form factors from Table II are characterized by the corresponding value of the monopole mass, m_M , implied by ($q^2 < 0$)

$$F_\pi(q^2) = \left(1 - \frac{q^2}{m_M^2}\right)^{-1}. \quad (29)$$

The m_M values arising from the form factors are divided by the measured m_ρ and displayed in Table III and Fig.9. Also shown are pion results from Ref. [3], which used 28 gauge field configurations of size $24^2 \times 12^2$ including an extra quark propagator with reversed momentum to decrease error bars. (Values and error bars for the pion and rho meson are extracted from the charge radius results in Table 1 of Ref. [3] using $m_M = \sqrt{6}/r$.) The result of our analysis is linearly extrapolated to the chiral limit; the χ_d^2 is 0.53. Our final result for the m_M/m_ρ ratio is 0.97(8). Note that the error bars on m_ρ are not included in the our results; this is not the conservative assumption. However, one reason for this is so our error bars can be compared with those in Ref. [3]. In addition, m_M and m_ρ are likely to be strongly correlated in both studies, so m_M/m_ρ is probably better determined than uncorrelated addition of the error bars would indicate. Also note that the physical q^2 of Ref. [3], set by the nucleon mass, is $|q^2| \approx 0.16 \text{ GeV}^2$. If we set our scale in the same fashion using the results of Ref. [16],

our physical momentum is $|q^2| \approx 0.47 \text{ GeV}^2$, approximately three times larger. Ref. [3] uses $\beta = 5.9$ as opposed to 6.0 here which means that the quark mass times lattice scale values, ma , from Ref. [3] must be multiplied by the ratio of scales so that we can compare results at the same physical quark mass value. (Ref. [3] uses Eq.(27) for ma .) The lattice scale in Ref. [16] is reasonably consistent within large errors with Ref. [3] using asymptotic scaling. The nucleon mass times the lattice scale, $m_N a$, was 0.54(3) in Ref. [16], as opposed to 0.59(6) in Ref. [3], giving the ratio of scales, $a(\beta = 5.9)/a(\beta = 6.0) = 1.09(13)$. Quenched asymptotic scaling would predict 1.12.

Let us make several additional points about the data sets shown in Fig.9. First, since the physical momentum in these two studies are so different, it is not required that the results be in agreement with one another at a given ma value. Second, since the earlier study did not use correlated χ^2 values to monitor the quality of their fits and because of the different lattice sizes and β values, a comparison between the error bars can not be made directly. Ref. [3] does not give chiral charge radii, but we will do a rough extrapolation of their implied $m_M/m\rho$ values in the next section to compare with ours. Third, the correlated fit shown in Fig.9 is quite different from what one would expect from an uncorrelated fit of the displayed error bars. Note that this is not a special result on the selected correlation time interval ($t = 14$ to 16), but occurs generally in our data whenever the same 3-time-slice interval is selected across all κ values.

Experimentally, a monopole form for the spacelike pion form factor gives an excellent fit to the data with, however, a pole mass about $4 \pm 1\%$ low compared to the mass of the rho [17]. This value was arrived at from the uncertainty in the fit pole mass given in the first paper in Ref. [17]: $736 \pm 9 \text{ MeV}$. (The value of the ρ^0 mass in the 1994 Particle Data Group review [18] is given as $768.1 \pm 1.3 \text{ MeV}$.) Note the agreement in the pole mass value in the two studies in Ref. [17] despite the difference in the studied $|q^2|$ ranges. Thus, it is encouraging that the chiral extrapolation of our results agrees in direction and approximate magnitude with the small naïve vector dominance violation seen in experiments. Of course, this may simply be fortuitous since our error bars are about twice the size of the experimental pole

mass shift.

In order to compare with the pion case, we again examine a monopole mass fit for the rho meson lowest momentum. Fig.10 shows the results and Table V lists the m_M/m_ρ ratios for the three κ values of this study. The linear chiral extrapolation of the data gives 0.73(10). The χ_d^2 for the correlated fit is 0.13. It is clear that the error bars here are significantly larger than for Ref. [3]. In addition, although both studies are low compared to vector dominance, our final extrapolation is about 2.7σ away from the expected vector dominance result of $m_M/m_\rho = 1$. Again, note our point above regarding the physical $|q^2|$ values of the two studies.

The last quantity we examine is the rho meson magnetic form factor, values of which are presented in Table IV. We note that although the conserved lattice current density is extended in space, the spatial separations used in the Fourier transform (see Eq.(11) above) are unambiguous since the Fourier transform is taken in directions perpendicular to the Lorentz index. Unlike the electric form factor, we have no absolute normalization for the $q^2 = 0$ value of $G_m(q^2)$. To help evaluate the significance of the data, we make the assumption that the electric and magnetic form factors have the same q^2 dependence for our range of momentum transfer. That is, independent of the unknown functional form, we simply assume (g_ρ is a constant in q^2)

$$\frac{G_m(q^2)}{G_c(q^2)} = g_\rho, \quad (30)$$

at each value of κ , and look at the dependence of g_ρ on the quark mass. In the nonrelativistic limit we expect that $g_\rho \approx 2$. The nonrelativistic quark model determines the magnetic moment in terms of the constituent quark mass, m_q , as

$$\mu_\rho = \frac{e}{2m_q}.$$

Experimentally, $\mu_\rho = g_\rho e/2m_\rho$, so that $g_\rho = m_\rho/m_q$, which is rendered less than 2 by the binding energy of the rho. See also Ref. [19] for a prediction from a light-front model, in excess of 2.

In Fig.11 and Table V we examine the g-factor that results. This quantity seems to approach it's final value from below. After doing a linear extrapolation, we find that $g_\rho = 2.25(34)$. The χ_d^2 on this correlated fit is 0.03.

In order to estimate the size of the finite lattice spacing systematic errors in this simulation, we used the lattice spin 0 dispersion relation [20]

$$\sinh^2\left(\frac{Ea}{2}\right) = \sinh^2\left(\frac{ma}{2}\right) + \sum_i \sin^2\left(\frac{p_i a}{2}\right), \quad (31)$$

and the normalized lattice propgator for a particle of mass m_M

$$F_\pi^L(q^2) \equiv \left(1 - \frac{\sinh^2\left(\frac{Ea}{2}\right) - \sum_i \sin^2\left(\frac{p_i a}{2}\right)}{\sinh^2\left(\frac{m_M a}{2}\right)}\right)^{-1}, \quad (32)$$

(the analog of Eq.(29)) to recalculate the fits in the correlation functions Eqs.(7)-(11) above. (The dimensionless mass parameter, \hat{M} , in Eq.(3.17) of Ref. [20] is related to the mass defined by the exponential falloff of the two-point function, \hat{m} by $\hat{m} = 2\sinh^{-1}\left(\frac{\hat{M}}{2}\right)$.) Also, we made the continuum to lattice replacements [21],

$$p_i \longrightarrow 2a^{-1} \sin\left(\frac{p_i a}{2}\right), \quad (33)$$

$$E \longrightarrow 2a^{-1} \sinh\left(\frac{Ea}{2}\right), \quad (34)$$

for the kinematic factors in these equations. The effect of these replacements was to decrease the chirally extrapolated monopole to rho mass ratio, m_M/m_ρ , by approximately 3.6% for the pion and 2.7% for the rho meson. The extrapolated rho meson g-factor was increased by 6.6% by these modifications.

To partially investigate the effect of inserting lower momentum, we evaluated the form factors at $\kappa = 0.152$ on lattices of size $20^3 \times 30$. These lattices were also generated at $\beta = 6.0$. They were thermalized by 5000 sweeps and separated by 1000 pseudo-heatbath sweeps. The measurements on these larger lattices were done as similar as possible to our $16^3 \times 24$ lattice measurements to provide a direct comparison. Using the same scale as before, the lowest momentum on these lattices is $|q^2| \approx 0.30 \text{ GeV}^2$, still about twice that in Ref. [3]. The dimensionless pion and rho masses measured using 50 configurations on $t = 15$ to 18 fits

($t = 0$ again labels the time origin) are given by 0.479(4) and 0.547(6), respectively. The form factors themselves were again measured with $t = 14$ to 16 fits on 10 of these lattices. We found $F = 0.80(3)$ and $G_c = 0.65(8)$, which gives $F/F^{VD} = 1.04(4)$ for the pion and $G_c/G_c^{VD} = 0.86(11)$ for the rho meson. When converted into an implied monopole mass, these results give $m_M/m_\rho = 1.09(11)$ for the pion and $m_M/m_\rho = 0.76(13)$ for the rho. The error bars on the m_M/m_ρ ratios increased significantly on the $20^3 \times 30$ lattices both because a smaller number of configurations were used and because standard error propagation shows that the relative error in the monopole mass is $\delta m_M/m_M = \delta F/[2F(1-F)]$ in terms of the form factor, F . The $(1-F)$ quantity in the denominator increases the error bars at lower momenta. However, comparing with the $\kappa = 0.152$ results in Tables III and V, we see that both m_M/m_ρ ratios have increased. This is what one expects if vector dominance is to be reinstated at lower $|q^2|$.

IV. SUMMARY AND COMMENTS

We have calculated the pion and rho meson form factors on a $16^3 \times 24$ lattice using the methods of current overlap. We limited our measurements to the lowest lattice momentum because of a possible violation of continuum dispersion seen in the pion local $(E - m)$ measurement. We have extracted a very clean pion signal which seems to be single exponential even near the time edges. In contrast, the rho meson electric signals are relatively noisy and seem to be more strongly affected by time-edge effects. We saw that the combined $Q(\pm; q_z^2, t)$ and $Q(0; q_{x,y}^2, t)$ values had a strong overlap with the $Q(\pm; q_{x,y}^2, t)$ results, consistent with a zero quadrupole form factor. However, because the correct exponential behavior in the latter quantity at $\kappa = 0.154$ and 0.152 was not demonstrated in the data, a signal for the quadrupole form factor could not be isolated. We also saw that the rho magnetic correlation functions, $K_y(+; q_x, t)$, develop faster in time than either the pion or rho electric ones, reminiscent of a result in Ref. [9]. Our error bars on the magnetic correlation function were encouraging; assuming Eq.(30), we extracted a rho meson g-factor and found $g = 2.25(34)$.

This value is consistent with the nonrelativistic quark model value of 2 and with the recent results of a light-front model [19].

Three sources of systematic error in our results were investigated. First, by comparing pion source time separations of $\Delta T = 17$ and 23, we saw no statistically significant difference in the time signals for the lowest momentum. We also found that the lattice was long enough to filter out the correct local $(E - m)$ for both the pion and rho meson. Second, by using the lattice spin 0 dispersion relation and definitions of kinematical factors, we saw that the physical m_M/m_ρ ratios for the pion and rho meson were decreased by 3.6% and 2.7%, respectively; the rho meson g-factor was increased by 6.6%. In addition, our results on the $20^3 \times 30$ lattices at $\kappa = 0.152$ gave larger values of m_M/m_ρ than the smaller lattices, but with larger error bars. Systematics associated with quenching and scaling have not been investigated and must wait future studies.

A comparison with the pion and rho results in Ref. [3] has been carried out. A simple uncorrelated linear extrapolation [22] of the Ref. [3] data displayed in Figs.9 and 10 yields a m_M/m_ρ ratio of 1.08(8) for the pion and 0.96(7) for the rho. (The CURFIT routine from Ref. [22] was used for the fit and error bars.) Our results for these same quantities are 0.97(8) and 0.73(10). If we combine errors in an uncorrelated fashion, Ref. [3] finds a rho meson to pion charge radius of 1.13(12), whereas our results give 1.33(21). The results in Ref. [3] were extracted at $|q^2| \approx 0.16 \text{ GeV}^2$, whereas here $|q^2| \approx 0.47 \text{ GeV}^2$. Figs.9 and 10 would seem to indicate a systematic difference in the m_M/m_ρ results at finite ma . However, both studies have chirally extrapolated results for the pion which are consistent with vector dominance and with one another, within large errors. On the other hand, our extrapolated rho meson m_M/m_ρ is approximately 2.7σ low compared to vector dominance, whereas Ref. [3] is consistent with the vector dominance prediction. We noted above that our $20^3 \times 30$ lattice results hint that the larger $|q^2|$ of the present study may be responsible for the differences seen.

It may help to put our results in the context of measurements of similar quantities in the baryon case. We are concentrating on the dimensionless quantity m_M/m_ρ in the present

work, similar to the dipole mass ratio m_D/m_N that was studied for the nucleon in Ref. [9]. On the same size of lattice as here, it was found in Ref. [9] that the m_D/m_N measurement was about 7% low compared to experiment after chiral extrapolation. The extrapolated g-factors there were about 10 – 20% smaller in magnitude than experiment. It is reasonable to expect there will be similar sized overall systematic errors on the m_M/m_ρ ratios and the rho meson g-factor in our case.

Comparison with the experimental results for the pion form factor [17] are suggestive of the finding of a small violation of naïve vector dominance in the spacelike pion form factor. Experimentally, the m_M/m_ρ ratio is 0.96(1). Clearly, the error bars on lattice studies must be significantly reduced before the results can begin to have phenomenological impact in this sector.

The simplest explanation for a small violation of naïve vector dominance in the pion form factor involves radially excited states of the rho⁵. Such physics is contained in the lattice simulation, even in the quenched approximation. Thus, it is conceivable that the nonzero ma results are indicative of this violation at our $|q^2|$. In any case, there must be additional physics, outside of naïve vector dominance influencing the pion and the rho, resulting in their different charge radii. Making stronger contact with these experimental issues will be a challenge for lattice QCD in the future and will require significantly larger statistics to probe closer to the chiral limit and to substantially reduce statistical error bars.

V. ACKNOWLEDGMENTS

This research was supported in part by NSF grant NSF-9401068. W. W. would like to thank the theory group at CEBAF and the Department of Physics, University of Kentucky, for their hospitality. The computations were carried out at the National Center for Supercomputing Applications and used the CRAY 2, CM5 and Power Challenge computers. We thank T. Draper for allowing us to use his Coulomb gauge fixed configurations and we acknowledge helpful conversations with K. F. Liu.

REFERENCES

- [1] T. Draper, R. M. Woloshyn, W. Wilcox, and K. F. Liu, *Nucl. Phys.* **B318** (1989) 319.
- [2] G. Martinelli and C. T. Sachrajda, *Nucl. Phys.* **B306** (1988) 865.
- [3] T. Draper, R. M. Woloshyn and K. F. Liu, *Phys. Lett.* **B234** (1990) 121.
- [4] W. Wilcox, *Phys. Lett.* **B289** (1992) 411.
- [5] D. B. Leinweber, T. Draper and R. M. Woloshyn, *Phys. Rev.* **D46** (1992) 3067.
- [6] W. Wilcox, in “Lattice 92” (J. Smit and P. Van Baal, Eds.) *Nucl. Phys. B* (Proc. Suppl.) **30** (1993) 491; W. Wilcox and B. Andersen-Pugh, in “Lattice 93” (T. Draper et. al., Eds.) *Nucl. Phys. B* (Proc. Suppl.) **34** (1994) 393.
- [7] W. Wilcox, *Phys. Rev.* **D43** (1991) 2443.
- [8] N. Cabibbo and E. Marinari, *Phys. Lett.* **119B** (1982) 387.
- [9] W. Wilcox, T. Draper and K. F. Liu, *Phys. Rev.* **D46** (1992) 1109.
- [10] T. Draper et. al., in “Lattice 88” (A. S. Kronfeld and P. B. Mackenzie, Eds.), *Nucl. Phys. B* (Proc. Suppl.) **9** (1989) 175.
- [11] S. Gottlieb, W. Liu, R. L. Renken, R. L. Sugar, and D. Toussaint, *Phys. Rev.* **D38** (1988) 2245.
- [12] B. Efron, *SIAM Review* **21** (1979) 460.
- [13] C. Bernard et. al., *Phys. Rev.* **D49** (1994) 2536.
- [14] C. Michael, A. McKerrell, *Phys. Rev.* **D51** (1995) 3745, and references therein.
- [15] G. P. Lepage, in “Lattice 91” (M. Fukugita et. al., Eds.) *Nucl. Phys. B* (Proc. Suppl.) **26** (1992) 45.
- [16] K. F. Liu, S. J. Dong, T. Draper and W. Wilcox, *Phys. Rev. Lett.* **74** (1995) 2172.

- [17] S. R. Amendolia et. al., *Nucl. Phys.* **B277** (1986) 168; E. B. Dally et. al., *Phys. Rev. Lett.* **48** (1982) 375.
- [18] L. Montanet et. al., *Phys. Rev.* **D50** (1994),
- [19] F. Cardarelli et. al., *Phys. Lett.* **B349** (1995) 393.
- [20] H. J. Rothe, “Lattice Gauge Theories - An Introduction”, p. 39, World Scientific, Singapore, 1992.
- [21] R. M. Woloshyn, T. Draper, K. F. Liu and W. Wilcox, *Phys. Rev.* **D39** (1989) 978.
- [22] P. R. Bevington, “Data Reduction and Error Analysis for the Physical Sciences”, McGraw-Hill, New York, 1969.
- [23] D. Bisello et. al., *Phys. Lett.* **B220** (1989) 321.

Footnotes

1. New techniques such as in S. J. Dong and K. F. Liu, *Phys. Lett.* **B328** (1994) 130, and Y. Kuramashi et. al., *Phys. Rev. Lett.* **72** (1994) 3448, are beginning to change the situation for the better.
2. We are grateful to T. Draper for telling us about this technique.
3. Note that it is always possible to fix a single spatial point in any n-point correlation function without introducing momentum smearing.
4. Such an assumption is implicit also in the results of Ref. [3] for the rho meson.
5. See for example Ref. [23] where two additional vector mesons with masses of about 1420 and 1770 MeV are sufficient to explain the timelike pion form factor data in the energy region $1.35 \leq \sqrt{s} \leq 2.4$ GeV.

TABLES

TABLE I. Hadron masses. χ_d^2 gives the chi-squared per degree of freedom for the fit.

Particle	$\kappa = 0.154$	0.152	0.148
pion	0.366(10)	0.479(8)	0.676(6)
χ_d^2	.45	.43	.28
rho	0.46(2)	0.55(1)	0.718(8)
χ_d^2	.23	.19	.05

TABLE II. Pion form factors for the lowest spatial momentum. F^{VD} indicates the vector dominance value for the lattice value of m_ρ from Table I. χ_d^2 gives the chi-squared per degree of freedom for the fit.

Quantity	$\kappa = 0.154$	$\kappa = 0.152$	$\kappa = 0.148$
F	0.58(4)	0.65(2)	0.74(3)
$\frac{F}{F_1^{VD}}$	0.91(7)	0.94(4)	0.94(3)
χ_d^2	0.65	0.20	1.02

TABLE III. Values of monopole mass divided by rho meson mass, m_M/m_ρ for the lowest momentum fit to the pion form factor. κ_c indicates the correlated chiral extrapolation.

κ_c	$\kappa = 0.154$	$\kappa = 0.152$	$\kappa = 0.148$
0.97(8)	0.89(6)	0.91(5)	0.89(6)

TABLE IV. G_c and G_m are the charge and magnetic form factors of the rho meson. G^{VD} indicates the vector dominance value for the lattice value of m_ρ from Table I. χ_d^2 gives the chi-squared per degree of freedom for the fit.

Quantity	$\kappa = 0.154$	$\kappa = 0.152$	$\kappa = 0.148$
G_c	0.46(6)	0.55(5)	0.68(4)
$\frac{G_c}{G^{VD}}$	0.74(9)	0.81(7)	0.87(6)
χ_d^2	0.43	0.33	0.23
G_m	0.93(15)	1.07(9)	1.14(7)
χ_d^2	0.79	0.83	0.79

TABLE V. m_M/m_ρ is the ratio of monopole mass to rho meson mass obtained from the G_c value for the rho meson. The g-factor assumes Eq.(30).

Quantity	κ_c	$\kappa = 0.154$	$\kappa = 0.152$	$\kappa = 0.148$
m_M/m_ρ	0.73(10)	0.73(8)	0.75(7)	0.77(8)
g-factor	2.25(34)	2.03(38)	1.93(21)	1.67(10)

Figure Captions

1. (a) Graphical representation of the four-point function being calculated. The time positions of the particle interpolation fields (shown as shaded circles) are fixed, but the charge and current densities, located on different flavor lines and symbolized by the “X”, may be time separated. (b) Example of a disconnected (sea quark) contribution. The disconnected quark loop is actually connected to the quarks by an arbitrary number of gluon lines.

2. (a) Fourier transform of pion charge overlap function at zero relative time separation, $Q(\vec{q}^2, 0)$, for smeared-to-smeared interpolation fields ($\kappa = 0.154$) as the charge densities are moved together in time between the sources. ($t = 0$ labels the first time slice of the lattice.) (b) Fourier transform of the same quantity for smeared-to-point interpolation fields. (The point interpolation field, located at $t = 24$, is unsummed.)

3. Comparison of pion overlap correlation function, $Q(\vec{q}^2, t)$, versus relative time separation, t , for a time separation $\Delta T = 17$ (squares) between the interpolation fields and a time separation of $\Delta T = 23$ (diamonds). Both calculations use smeared-to-smeared quark propagators with $\kappa = 0.154$.

4. Local $(E - m)$ measurements for the pion overlap function, $Q(\vec{q}^2, t)$, versus relative time separation, t , compared with continuum dispersion for (a) $|\vec{q}_{min}| = \frac{\pi}{8}$ and (b) $|\vec{q}| = \sqrt{2}|\vec{q}_{min}|$. Squares are $\kappa = 0.154$, triangles are $\kappa = 0.152$, and circles are $\kappa = 0.148$ results. Continuum dispersion is indicated by the solid lines; the associated spin 0 lattice dispersion relation is indicated by dotted lines underneath.

5. Correlation functions, $Q(\vec{q}^2, t)$, for the lowest spatial momenta ($|\vec{q}| = \frac{\pi}{8}$) of the pion versus relative time separation, t . Results are at $\kappa = 0.148$ (circles), $\kappa = 0.152$ (triangles) and $\kappa = 0.154$ (squares). (The kinematical factor $\frac{(E_q + m_\pi)^2}{4E_q m_\pi}$ has been removed from $Q(\vec{q}^2, t)$.) The best uncorrelated single exponential fits on the 14-16 time interval are shown.

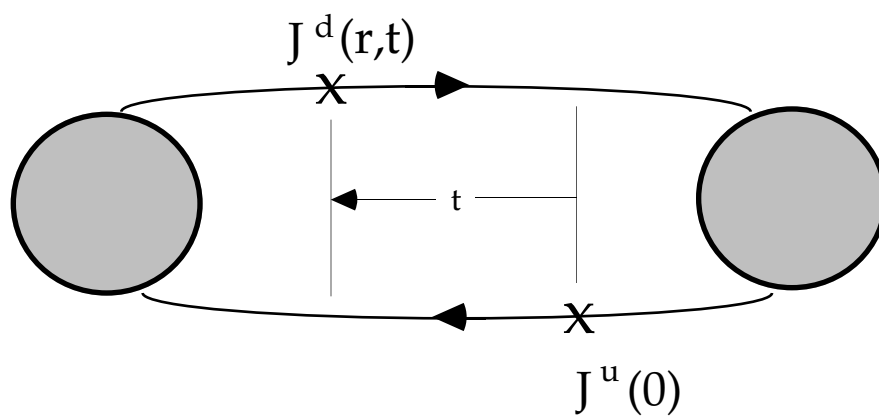
6. The electric correlation function $Q(\pm; q_z^2, t)$ for the rho meson for the lowest spatial momenta ($|\vec{q}| = \frac{\pi}{8}$) versus relative time separation, t . Results are at $\kappa = 0.148$ (circles), $\kappa = 0.152$ (triangles) and $\kappa = 0.154$ (squares). (The kinematical factor $\frac{(E_q+m_\rho)^2}{4E_q m_\rho}$ has been removed from $Q(\pm; q_z^2, t)$.) The best single exponential fits on the 14-16 time interval are shown for $\kappa = 0.148$ and 0.152; the best fit for the 13-15 interval is shown for $\kappa = 0.154$.
7. The magnetic correlation function $K_y(+; q_x, t)$ for the rho meson for the lowest spatial momentum ($|\vec{q}| = \frac{\pi}{8}$) versus relative time separation, t . Results are at $\kappa = 0.148$ (circles), $\kappa = 0.152$ (triangles) and $\kappa = 0.154$ (squares). (The factor $i q_x \frac{(E_q+m_\rho)}{4E_q m_\rho}$ has been removed from $K_y(+; q_x, t)$.) The best single exponential fits on the 7-9 time interval are shown.
8. The quadrupole correlation function $Q_\rho(\pm; q_{x,y}^2, t)$ for the rho meson for the lowest spatial momentum ($|\vec{q}| = \frac{\pi}{8}$) versus relative time separation, t . (The kinematical factor $\frac{(E_q+m_\rho)^2}{4E_q m_\rho}$ has been removed.) Results are at $\kappa = 0.148$ (circles), $\kappa = 0.152$ (triangles) and $\kappa = 0.154$ (squares). No fits of these functions were made.
9. Monopole mass divided by the rho meson mass, m_M/m_ρ , for the pion as a function of dimensionless quark mass (ma) as determined from the lowest momentum measurements (squares). The darkened square gives the chiral extrapolation. The triangles give results extracted from Table 1 of Ref. [3].
10. Monopole mass divided by the rho meson mass, m_M/m_ρ , for the rho meson as a function of dimensionless quark mass (ma) as determined from the lowest momentum measurements (squares) assuming the quadrupole form factor is zero. The darkened square gives the chiral extrapolation. Triangles are the results extracted from Table I of Ref. [3].
11. g-factor for the rho as a function of dimensionless quark mass (ma) assuming Eq.(30). Darkened square gives the chiral extrapolation.

This figure "fig1-1.png" is available in "png" format from:

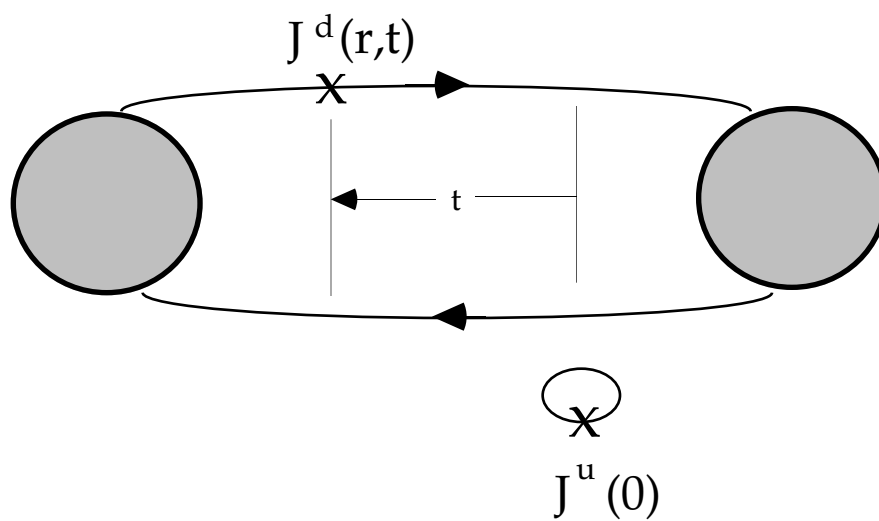
<http://arxiv.org/ps/hep-lat/9502015v2>

This figure "fig2-1.png" is available in "png" format from:

<http://arxiv.org/ps/hep-lat/9502015v2>



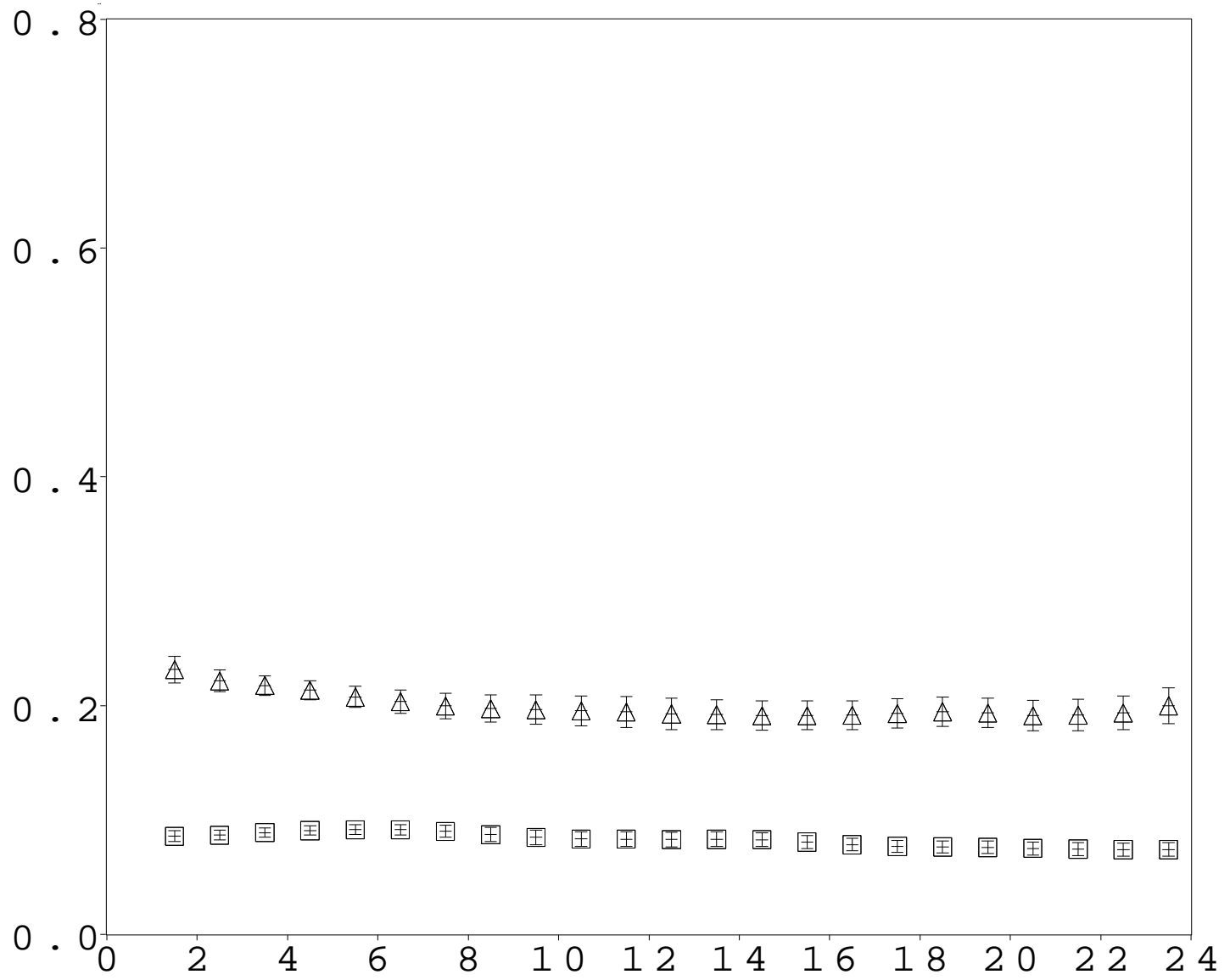
(a)

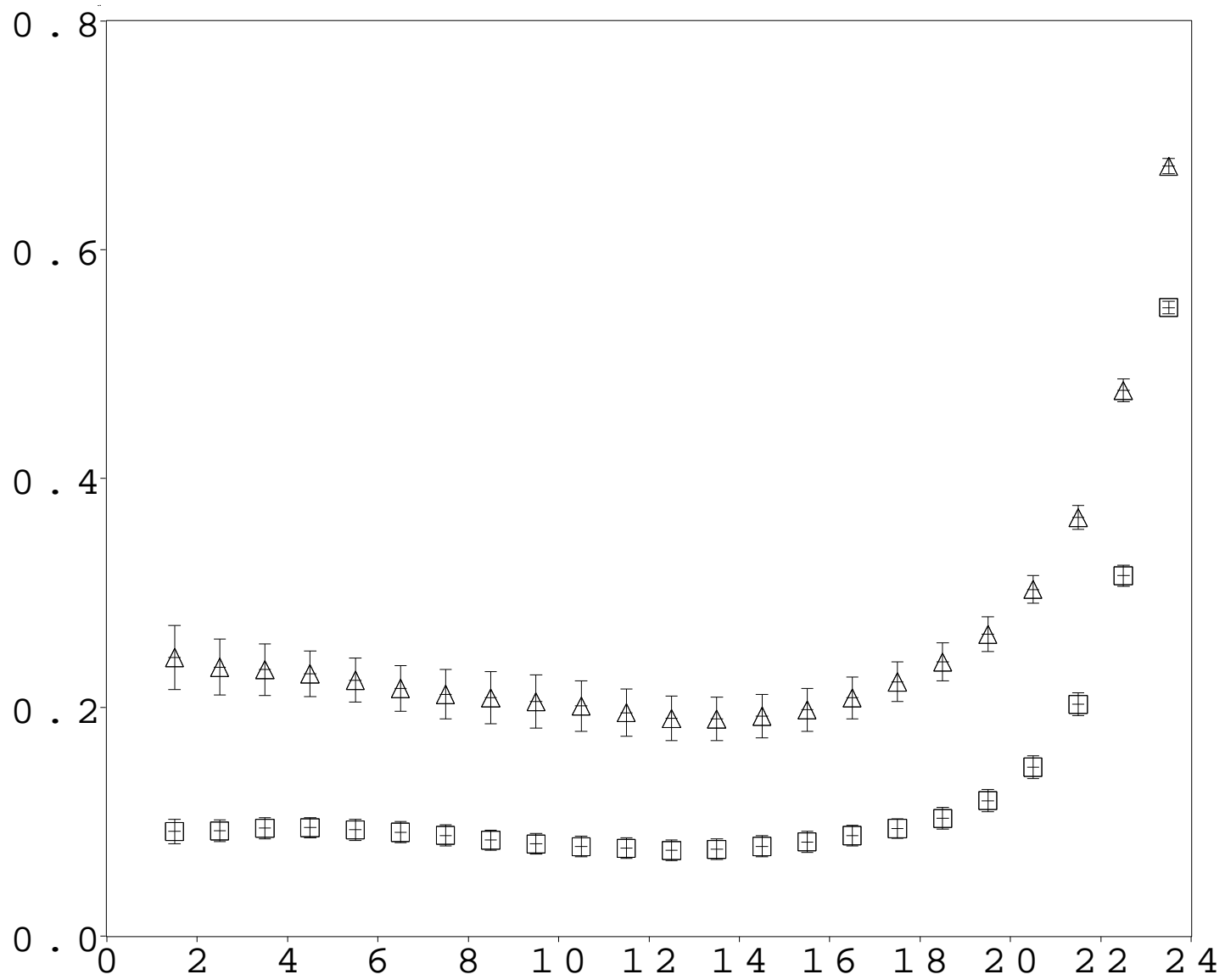


(b)

This figure "fig2-2.png" is available in "png" format from:

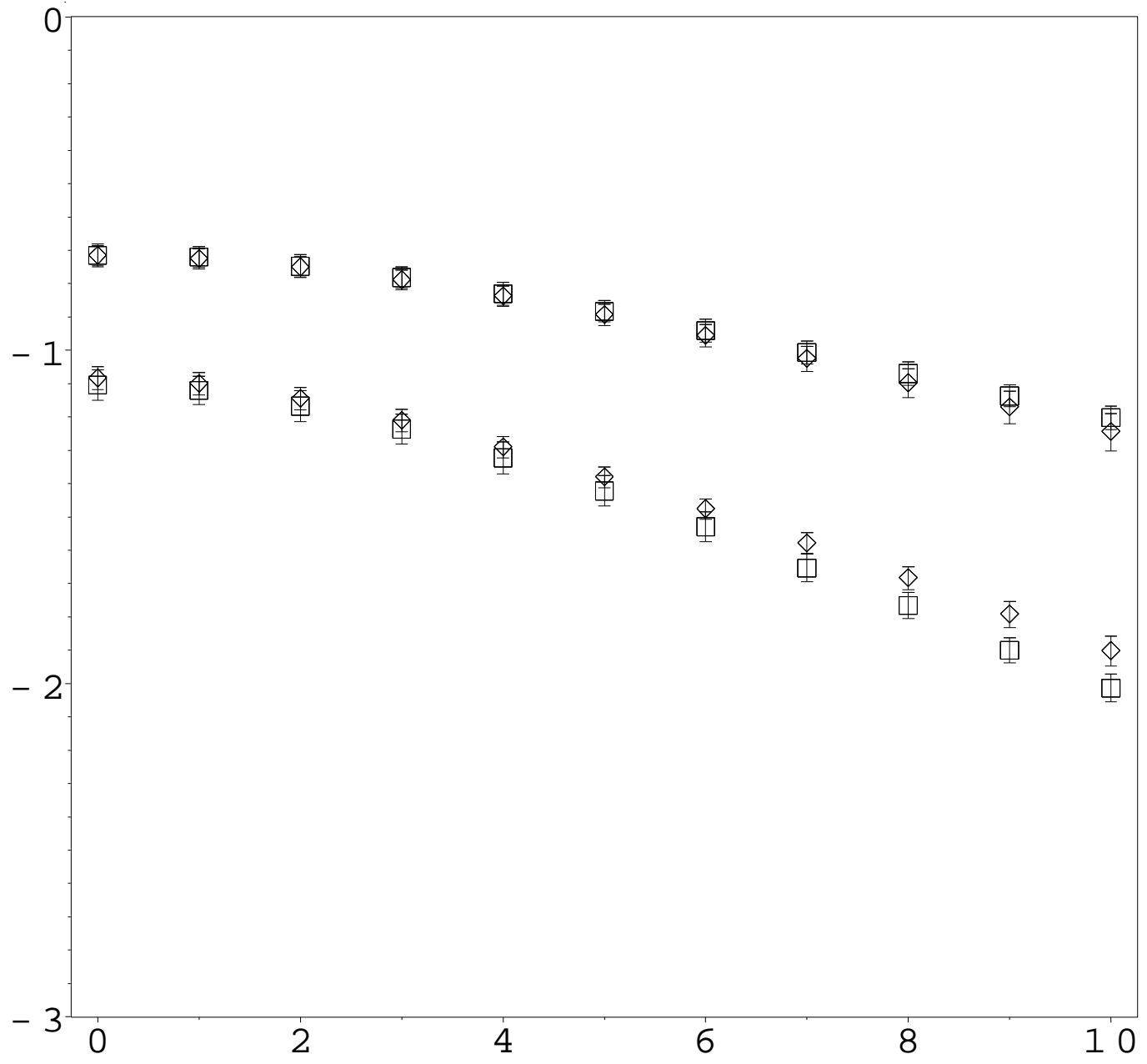
<http://arxiv.org/ps/hep-lat/9502015v2>





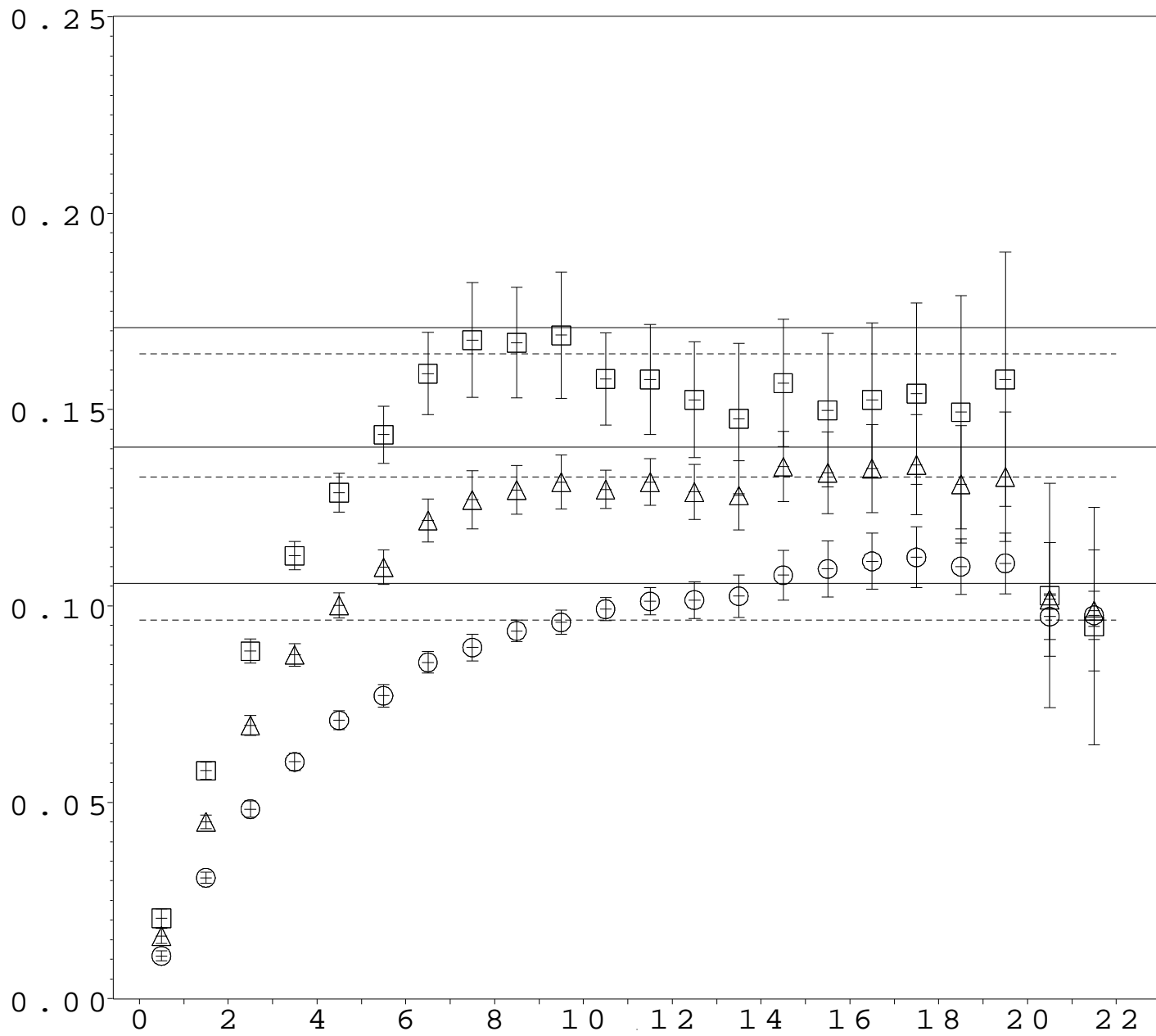
This figure "fig2-3.png" is available in "png" format from:

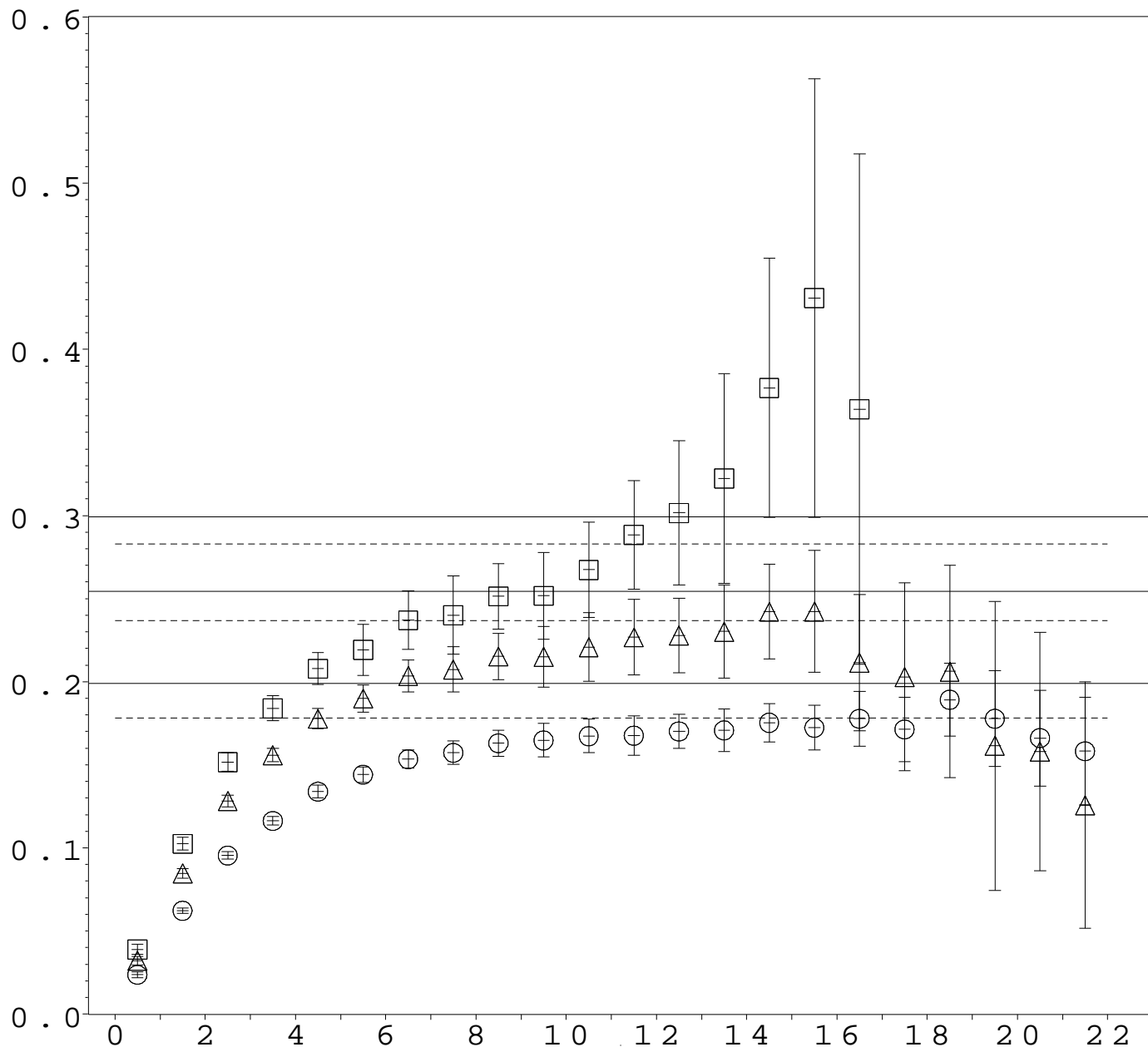
<http://arxiv.org/ps/hep-lat/9502015v2>



This figure "fig2-4.png" is available in "png" format from:

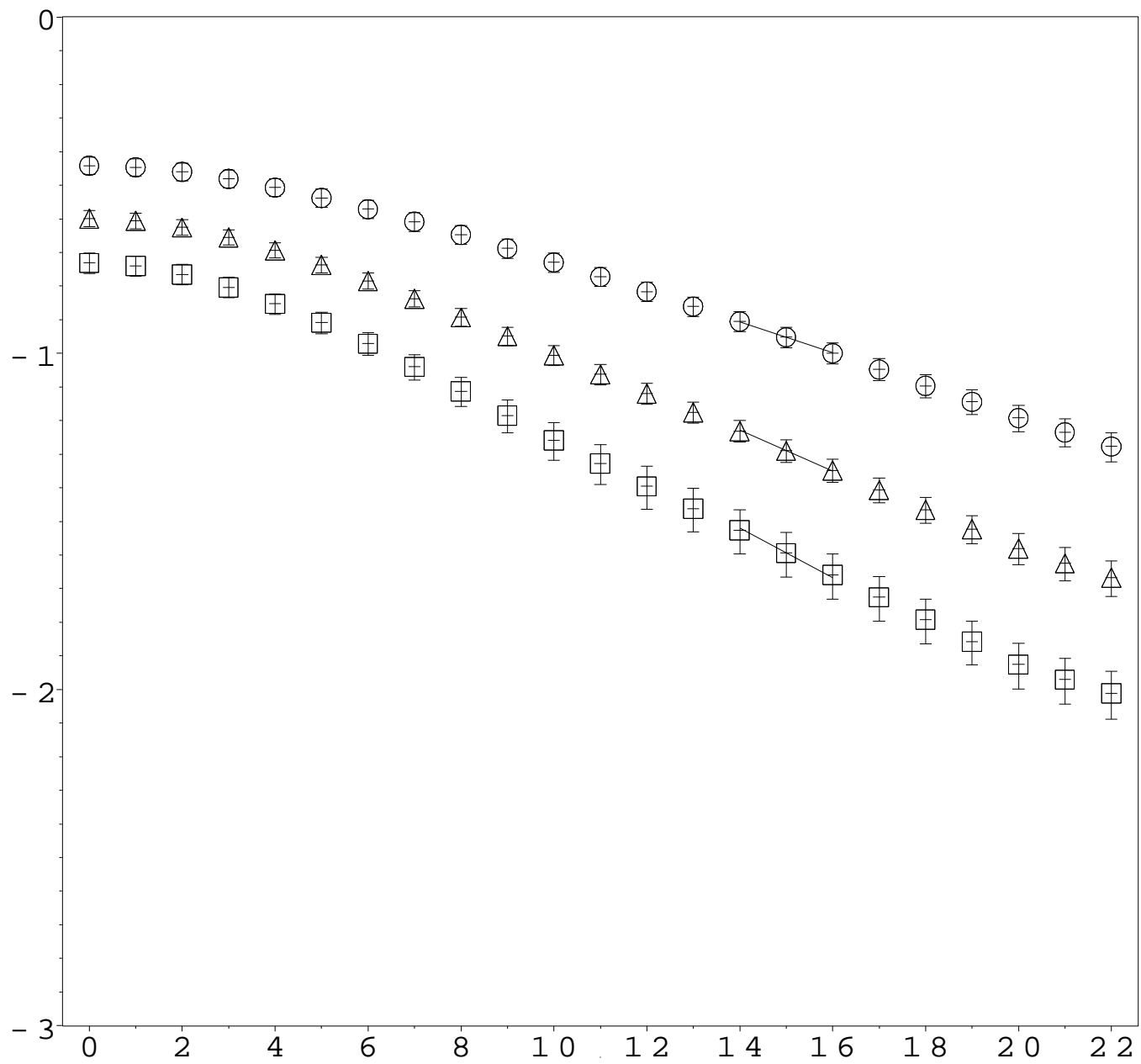
<http://arxiv.org/ps/hep-lat/9502015v2>





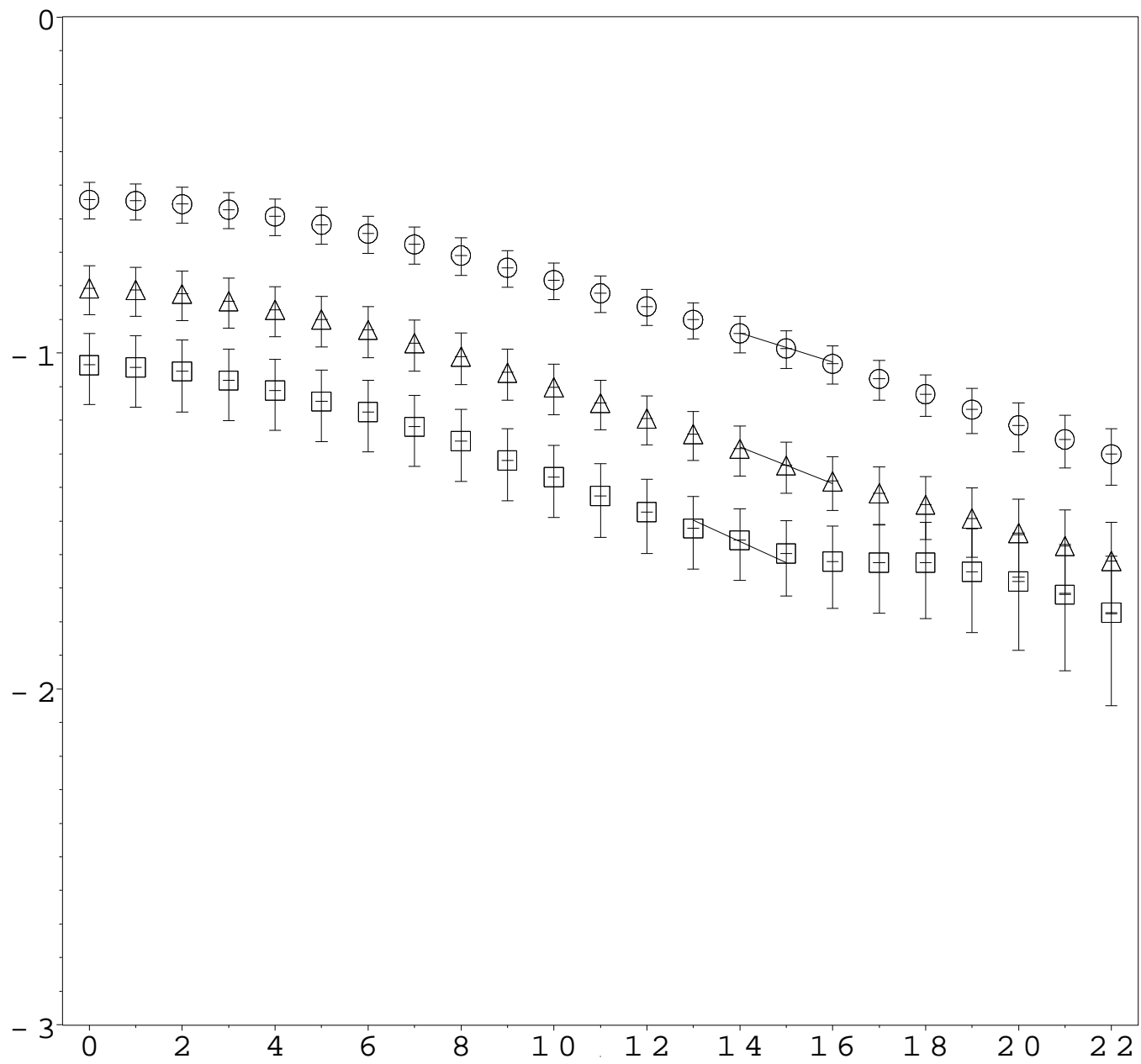
This figure "fig2-5.png" is available in "png" format from:

<http://arxiv.org/ps/hep-lat/9502015v2>



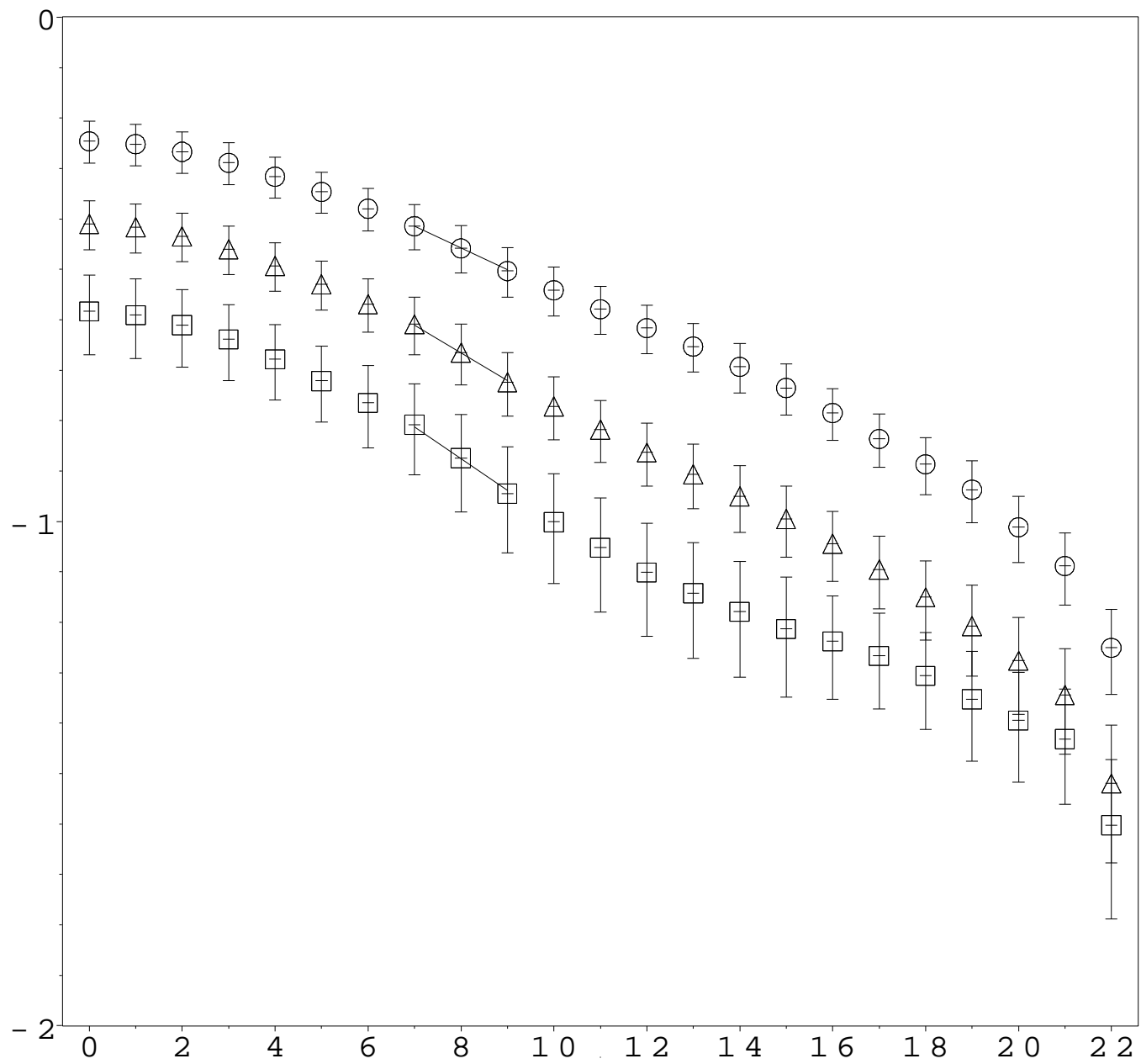
This figure "fig2-6.png" is available in "png" format from:

<http://arxiv.org/ps/hep-lat/9502015v2>



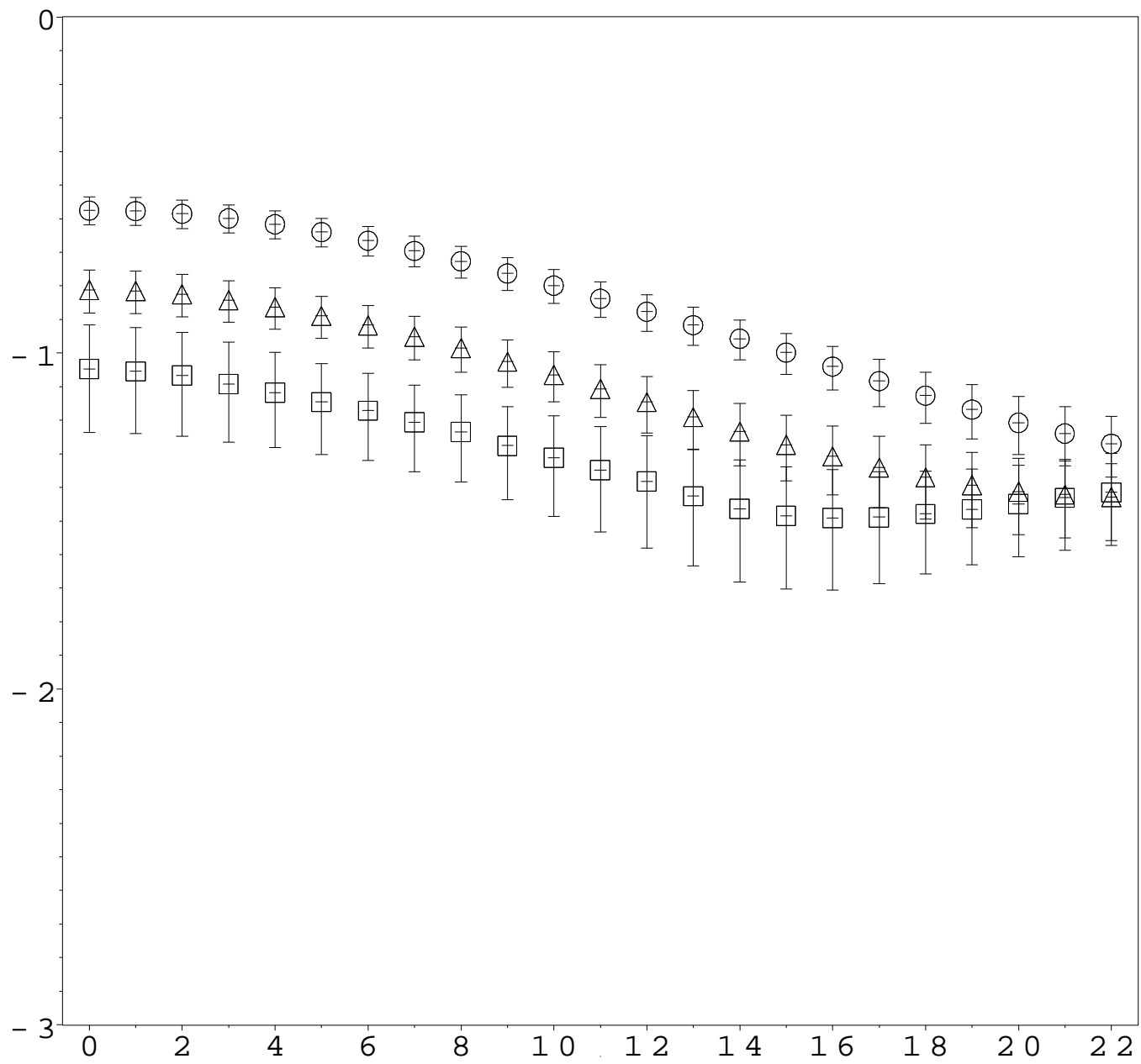
This figure "fig2-7.png" is available in "png" format from:

<http://arxiv.org/ps/hep-lat/9502015v2>



This figure "fig2-8.png" is available in "png" format from:

<http://arxiv.org/ps/hep-lat/9502015v2>



This figure "fig2-9.png" is available in "png" format from:

<http://arxiv.org/ps/hep-lat/9502015v2>

